Journal of Fluids and Structures 23 (2007) 1029–1046

JOURNAL OF
FLUIDS AND
STRUCTURES

www.elsevier.com/locate/jfs

# Unsteady pressure in the annular flow between two concentric cylinders, one of which is oscillating: Experiment and theory

A. Mekanik[a,*], M.P. Païdoussis[b]

[a]*Department of Mechanical Engineering, Bu-Ali Sina University, Mehdieh Avenue, Hamadan 65174, Iran*
[b]*Department of Mechanical Engineering, McGill University, Montreal, Qué., Canada H3A 2K6*

Received 13 February 2006; accepted 24 March 2007
Available online 15 June 2007

## Abstract

The first objective of this paper is to present a series of accurate experimental measurements of the unsteady pressure in the annulus between two concentric cylinders, the outer one of which executes a harmonic planar motion, either transverse translational or rocking motion about a hinge, with and without annular flow. The second objective is the solution of the unsteady Navier–Stokes and continuity equations for the same annular geometry under the same boundary conditions for an incompressible fluid in the laminar regime. The solutions are obtained with a three-time-level implicit integration method in a fixed computational domain by assuming small amplitudes of oscillation of the outer cylinder. A pseudo-time integration method with artificial compressibility is used to advance the solution between consecutive real time levels. The finite difference method is used for spatial discretization on a stretched staggered grid. The problem is reduced to a scalar tridiagonal system, solved by a decoupling procedure which is based on a factored Alternating Direction Implicit (ADI) scheme with lagged nonlinearities. The third objective is the comparison of the experimental results with the theoretical ones. This comparison shows that the two are in good agreement in the case of translational motion, and in excellent agreement in the case of rocking motion. The experimental and theoretical work presented in this paper is useful for fluid–structure interaction and flow-induced vibration analyses in such geometries.

*Keywords:* Annular flow; Unsteady pressure; Concentric cylinders; Oscillating boundaries; Theory; Experiment

## 1. Introduction

Cylindrical structures subjected to either internal, external or annular flows are found in many engineering constructions, particularly in the power-generating, chemical, and petrochemical industries, e.g., in the form of piping of all kinds, marine risers, and chimneys; fuel pins, monitoring and control rods in nuclear reactors; heat exchanger tube arrays and bundles of electrical conductors in transmission lines; and thin walled shrouds and flow-containment shells in nuclear reactors, aircraft engines, and jet pumps; to name but a few of the most familiar such systems (Païdoussis, 1980, 1998, 2003).

The instabilities associated with internal and external axial flows are of limited practical concern for conventional engineering systems. This is not the case with instabilities associated with annular flows. The analysis of unsteady

---

*Corresponding author. Tel.: +98 811 8224256; fax: +98 811 8257400.
*E-mail address:* Meka47ir@Yahoo.com (A. Mekanik).

doi:10.1016/j.jfluidstructs.2007.03.003

confined flows with oscillating boundaries has recently elicited an increased research interest for its application to numerous engineering problems, which explains the enhanced interest for the analysis of unsteady annular flows with oscillating boundaries.

Unsteady annular flows between cylindrical structures executing transverse oscillation have been studied theoretically (via simplified theoretical models) and experimentally by numerous researchers. The first attempt to explain the mechanism underlying annular-flow-induced instabilities is due to Miller (1970), and the first analytical model for the cylindrical geometry was developed by Hobson (1982). This problem has been seriously studied by, among others, Chen et al. (1976), Mateescu and Païdoussis (1985), Mateescu et al. (1988) and Inada and Hayama (1990). These simplified theoretical models were proven to give predictions in good agreement with experimental results, at least for simple cylindrical structures (Mateescu et al., 1989).

For more realistic and complex geometries, insofar as the analysis of unsteady viscous flow in annuli with oscillating boundaries is concerned, there was a need for more accurate experimental measurements of the unsteady forces and accurate solutions based on the time-accurate integration of the full nonlinear Navier–Stokes equations. One such attempt was made by Mateescu et al. (1994a, b), who used a computational method to integrate the linearized Navier–Stokes (N–S) equations for small amplitude oscillation of the outer cylinder. Inherent in the computational methods developed for this purpose was a high degree of accuracy and computational efficiency, necessary for the simultaneous time-integration of the Navier–Stokes equations and the structural equations of motion, as required in the study of the fluid–structure interaction (Mekanik et al., 1993; Mekanik, 1994; Mateescu et al., 1996).

Experimental measurements of the unsteady pressure on the annulus walls or the unsteady forces exerted on either the inner or outer cylinder, Fig. 1, have been made in the past in turbulent flows, for the purposes of design or validation of existing theoretical models [Spurr and Hobson (1984); Mateescu et al. (1988), $32\,000 \leqslant \mathrm{Re} \leqslant 45\,000$; Mekanik et al. (1994), $3000 \leqslant \mathrm{Re} \leqslant 20\,000$]. In contrast, no experiments were conducted for unsteady laminar flows, which may be practically important, especially in very narrow annuli.

To study any fluid–structure interaction problem, one may use either an experimental or a theoretical (analytical or numerical) approach, or a combination of the two. On the theoretical side, for an analytical solution, a number of simplifying, often undesirable, assumptions need generally be made to render the problem tractable. Numerical methods, on the other hand, have the advantage of flexibility. Furthermore, either type of theoretical analysis has the following advantage *vis-à-vis* experiment: there are few inaccessible locations for computation, and no unwanted effects due to disturbances caused by probes, bolts, support rods, etc. The main advantage of an experimental investigation is that it studies reality itself. It has the disadvantage of being confined to measurement of a few variables, at judicious locations. Therefore, if an experimental study is undertaken, it would generally benefit from a companion numerical analysis which would supplement it. This, in fact, is the approach adopted in this paper.

There has been a great deal of work in the late 1990s on various aspects of vibrations and instabilities involving annular flows that should be mentioned. On the experimental side, a large-scale programme utilizing the TAXI apparatus (de Langre et al., 1994) was conducted on the stability of a cylindrical-conical centre-body and an oscillating outer cylindrical pipe with annular flow upstream and diffuser-type flow in the downstream portion. Some combined theoretical–experimental work, also involving the stability of a conical centre-body, was conducted by Arai and Tajima (1998), the theoretical model being in the spirit of Inada and Hayama's (1990). This type of work was taken further by Arai and Tajima (1999) and Li et al. (2002). Also, a train of interconnected cylinders in a tunnel (hence involving an equivalent annular flow) has been studied by Tanaka et al. (2001).

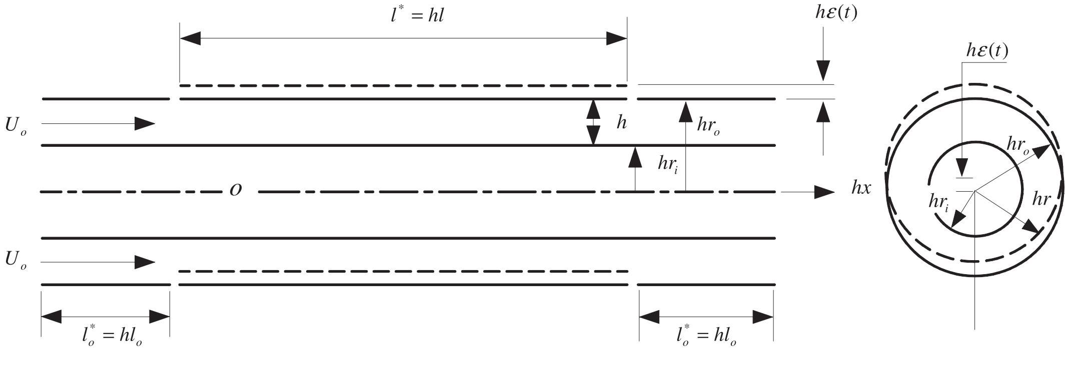

Fig. 1. Geometric representation of uniform annular passage with oscillating middle section of the outer cylinder.

On the theoretical side, semi-empirical models were developed by Fujita et al. (1994), who reexamined essentially the problem first studied by Hobson, and by Porcher and de Langre (1997), as well as the work just mentioned (Arai and Tajima, 1999; Li et al., 2002). A very powerful numerical model involving linearized unsteady fluid dynamics for fluid–structure interactions between annular flows and vibrating structures (the MOCCA code) was developed in France; it involves little empirical input. It was utilized by Perotin and Granger (1997) to study the stability of systems such as those in the aforementioned TAXI experiments, achieving remarkably accurate predictions.

The interested reader can find a review of all the pertinent work in Païdoussis (2003, Chapter 11), including work involving annular flows and coaxial shells. Sample results from Mekanik's (1994) work, reported in detail in the present paper, are also presented therein.

The ultimate aim of this study is to validate the analytical model developed by Mekanik et al. (1993) and Mateescu et al. (1994a) in laminar flow, if this proves possible. For this purpose, first the experimental programme for measuring unsteady wall-pressures in cylindrical annuli will be presented. Then, the numerical model developed by Mekanik (1994) for the analysis of unsteady confined flows with oscillating walls, based on the accurate time-integration of the Navier–Stokes equations, is described. Finally, the experimental measurements are compared to the theoretical predictions. Once the model is validated, it then becomes possible to couple the fluid-dynamics model with the equation of motion of the rigid or flexible inner or outer cylinder (the motion of which is no longer prescribed), and a stability analysis can then be conducted [see, e.g., Bélanger et al. (1994), Mekanik (1994)].

## 2. Experimental investigation

In the present study, a special apparatus was constructed, the general layout of which is shown in Fig. 2. With this apparatus, rocking and lateral (translational) motions of part of the outer conduit are equally feasible, while the cylindrical centre-body remains immobile.

To reduce such viscous-flow effects as flow separation and vortex shedding, neither of which is considered in the numerical solution, a smooth transition between cylindrical and annular flow is desirable both upstream and downstream. To this end, smooth ogives are mounted at the ends of the fixed centre-body, as shown in Fig. 2. The constant cross-section segment, from the upstream ogive to the test-section, where the pressure was measured, is long enough to obtain fully developed laminar flow. The tests have been conducted at low amplitudes of oscillation, characterized by an amplitude/gap ratio smaller than 0.2. The tests were performed in air-flow.

### 2.1. Experimental apparatus

The test-section consists of a rigid cylindrical centre-body with ogival ends, concentrically located in a cylindrical conduit; see Fig. 2. The ogives, together with an upstream meshed screen and a honeycomb help to make the annular flow fully developed laminar and as uniform as possible. Since the central portion of the outer tubular aluminium cylinder is forced to oscillate, there will always be discontinuities at the boundaries between the oscillating portion of the outer cylinder and its immobile upstream and downstream extensions. A great deal of time was spent on this effect. The "obvious" solution of using flexible thin rubber sleeves to connect the two was found unsatisfactory, from the mechanical point of view: the sleeves had bias either in shape or in locked-in stresses which affected the uniformity of motion in the case of transverse oscillation (by "pulling" at the extremities of the oscillating cylinder). With zero-mean-flow experiments, any of the arrangements in Fig. 3(c) performed satisfactorily. With flow, however,

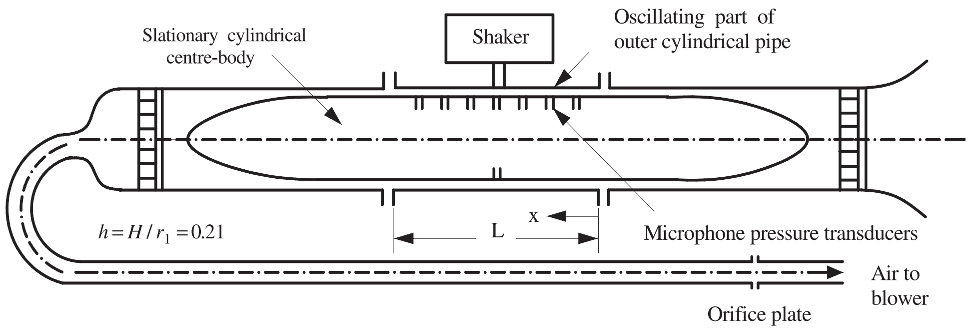

Fig. 2. Schematic representation of the experimental apparatus.

especially at relatively high Reynolds number, arrangement (i) at the far left of Fig. 3(c) with sponge-felt gaskets was by far the best.

The unsteady pressure was measured using eight PCB 103A11 and 103A12 pressure transducers (microphones) situated at $x/L = 0.263$, 0.342, 0.421, 0.500, 0.578, 0.657 and 0.763, in the vertical plane of oscillation, as shown in Fig. 3(a). The arrangement for mounting the pressure transducers is shown in Fig. 3(b). At the mid-point, two transducers were located diametrically opposite each other in order to compare the corresponding measured unsteady pressures and the phase angle relative to the imposed oscillation.

In the case of translational motion, the oscillatory motion was transmitted to the cylinder by a yoke placed around the midpoint $X = x/L = 0.5$ (Fig. 4(a)). For rocking motion, the oscillation about a "hinge" ($X = 0.237$) was transmitted via a flexible thin plate attached to the shaker at $X = 0.815$ (Fig. 4(b)).

The outer conduit was oscillated by means of a Brüel & Kjaer electromagnetic shaker (exciter body B&K 4801, with exciter head B&K 4812). The maximum peak-to-peak amplitude limit was 12.7 mm and the maximum force rating was 445 N; the possible frequency range was from 5 Hz to 10 kHz. The shaker was controlled through a feedback loop by an exciter control unit (B&K 1047) and power amplifier (B&K 2707), as shown in Fig. 5.

An accelerometer (B&K 4381) was mounted on the outer pipe for measuring the displacement of the oscillating cylinder as well as the phase angle between the unsteady pressure signal and the acceleration signal, as shown in Fig. 5.

The signals from the pressure transducers (one at a time) and the accelerometer, after suitable conditioning (using charge amplifier B&K 2624 and pressure signal amplifier PCB 483AO7), were fed into a dual channel FFT digital spectrum analyzer (HP 3582A). These signals could be post-processed, as desired, by a PC computer incorporating an HP–IB interface card, as shown in Fig. 5. The root-mean-square amplitude of the pressure and acceleration at the

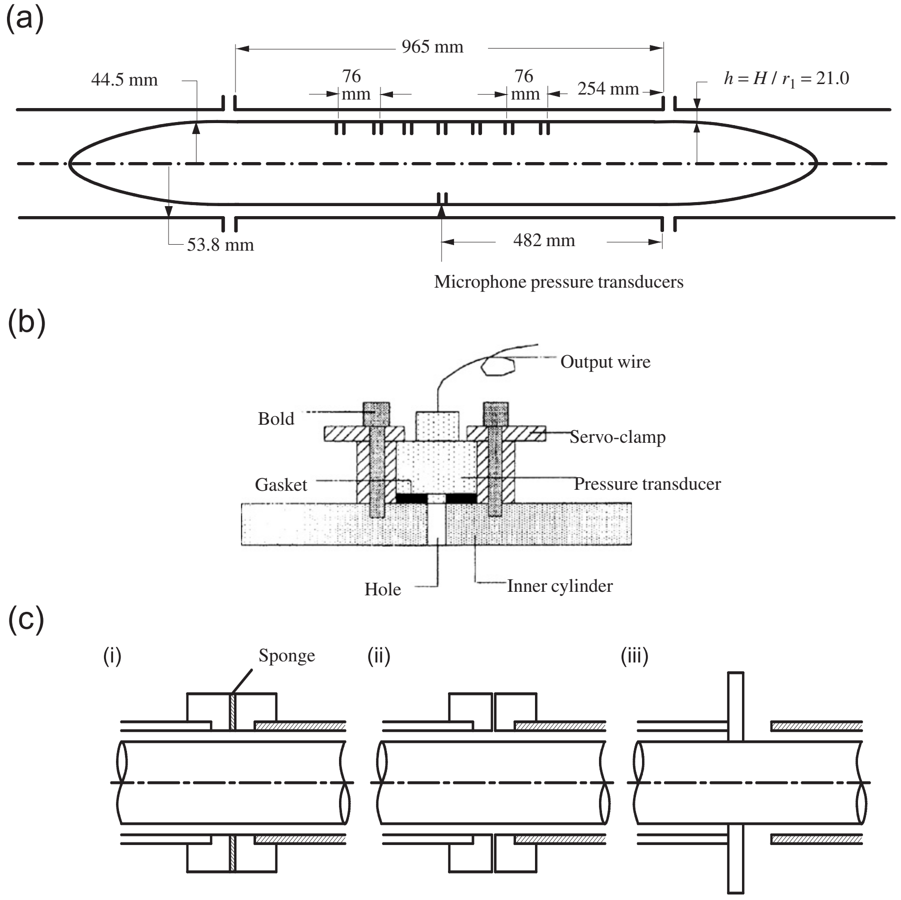

Fig. 3. (a) Dimensions of the apparatus and location of pressure transducers. (b) Mounting arrangement of the pressure transducers inside the centre-body. (c) Sealing arrangements between the moving and stationary parts of the outer cylinder: (i) sponge rings between flanges; (ii) close-fitting flanges; (iii) flange with rubbing contact (for zero axial flow only).

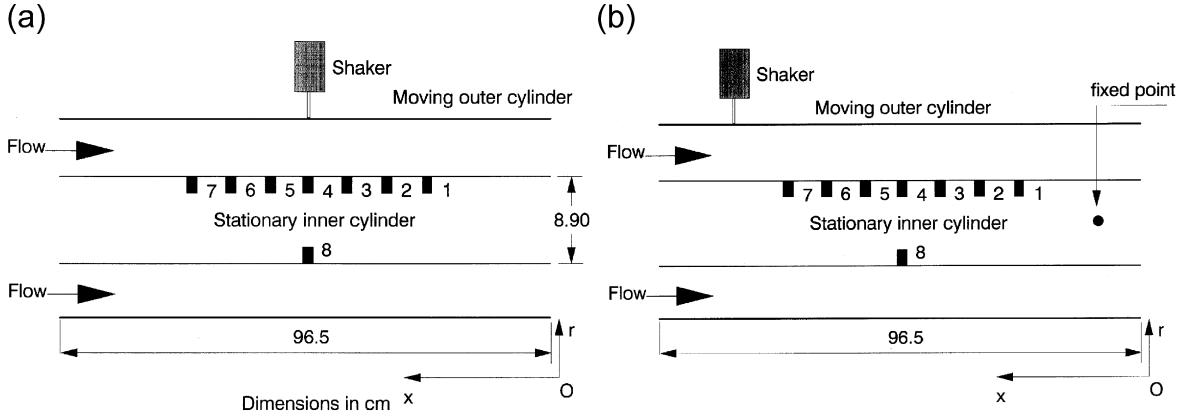

Fig. 4. Schematic diagram of the centre-body, the outer cylinder, the shaker and the pressure transducers: (a) translational motion; (b) rocking motion of the outer cylinder.

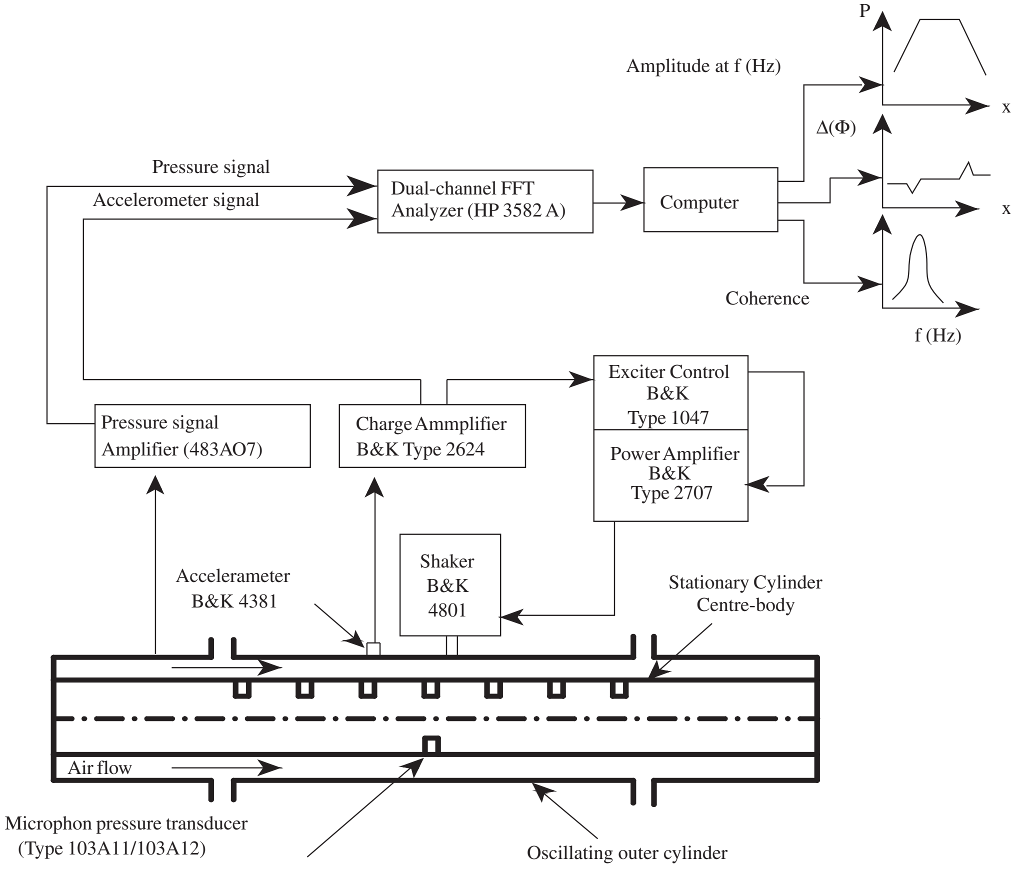

Fig. 5. Schematic diagram of the experimental apparatus and measurement system.

oscillation frequency were obtained from the corresponding spectra (typically with 16 averages). The phase difference of the pressure relative to the acceleration was determined with the analyzer operating in transfer-function mode. It should be mentioned that, in most cases, the signals contained superharmonics of the basic frequency; in what is presented in this research a linear analysis is undertaken, and only the components at the principal frequency are considered.

The air-flow was provided by a vacuum pump (used in suction mode), providing a laminar flow. The flow velocity was measured by orifice plates.

Utilizing the present apparatus, the following parameters are varied in the experiments: (a) oscillation frequency; (b) oscillation amplitude; (c) axial flow velocity.

### 2.2. Measured quantities

The flow rate was measured by means of several orifice plates (depending on the flow rate) of different size; they were checked against one another using the appropriate equations, thus confirming that the orifice plates could be used with confidence. The orifice plate was mounted near the downstream end of a straight pipe (3 m long and 40 mm in diameter), as shown in Fig. 2. This length is required to obtain fully developed flow upstream of the orifice plate.

The FFT spectrum analyzer is capable of providing the amplitude of either the accelerometer signal or the pressure signal at the frequency of oscillation in the form of a power spectrum. The phase difference between the pressure and acceleration could similarly be obtained from the cross-spectrum of these quantities as well as the coherence which is obtained directly, as shown in Fig. 5. By measuring the coherence, one can make sure that the pressure signals obtained are due to the oscillation of the outer cylinder and are not due to external sources such as acoustic noise or vibration of the centre-body. The main advantage of using the FFT analyzer was that the signal associated with secondary effects (e.g. the nonlinearity of the fluid motion, possible unexpected secondary motions of the cylinders, flow disturbances, and acoustic wave pressure components) can adequately be separated from the signal.

The pressure transducers were calibrated, one at a time, against a PCB 106B pressure transducer of known sensitivity (43.51 mV/kPa, with a resolution of 0.69 Pa) with the aid of a special device. Using the reference signal from this transducer, the sensitivities of the actual pressure transducers were found to be in the range of 53.9–93.7 mV/kPa. The accelerometer was calibrated with the aid of an accelerometer calibration exciter (B&K 4294), the acceleration of which is fixed (10 m/s$^2$ at 159.2 Hz). The sensitivity of the accelerometer (B&K 4381) was found to be 1.02 mV/m/s$^2$.

### 2.3. Experimental procedure

The experiment was started by first setting the amplitude of oscillation, for example 1 mm peak-to-peak, on the exciter control. Then, the frequency, for instance 20 Hz, was set. The shaker was turned on and the magnitude of the r.m.s. value (with 16 averages) of the pressure on the FFT analyzer was read for two pressure transducers, since the analyzer is dual-channel. Then, the next two transducers were selected by using a selector switch and the readings were recorded by the computer.

To measure the phase angle, one of the channels of the analyzer was connected to the accelerometer, while the other was connected to the selected pressure transducer via the selector switch. The mode of the analyzer was changed from the one for amplitude reading to that for phase reading. The phase angles for all the transducers were recorded in the same way as for pressure measurement. The corresponding coherence was then measured, following a similar procedure.

For any individual experiment, if there was any doubt in the results or in the experimental environment, the experiment was repeated several times to obtain through appropriate averaging the most accurate results possible. Another important test to ensure more accurate results was to interchange the pressure transducers. This eliminated doubts that the readings of some of the transducers were influenced by the local geometrical configuration, the mounting, or set screws, support rods, pins, etc., which were used inside the annulus for rigidity.

## 3. Numerical method

### 3.1. Formulation of the method

The incompressible time-dependent Navier–Stokes and continuity equations in 3-D cylindrical coordinates can be expressed in nondimensional conservation-law form as

$$\frac{\partial \mathbf{V}}{\partial \mathbf{t}} + \mathbf{Q}(\mathbf{V}, p) = \mathbf{0}, \quad \nabla \cdot \mathbf{V} = \frac{\partial u}{\partial x} + \frac{\partial v}{\partial r} + \frac{1}{r}\frac{\partial w}{\partial \theta} = 0, \tag{1}$$

where $\mathbf{V} = [u, v, w]^{\mathrm{T}}$ is the nondimensional velocity vector, and the vector $\mathbf{Q}(\mathbf{V}, p) = [Q_u(u, v, w, p), Q_v(u, v, w, p), Q_w(u, v, w, p)]^{\mathrm{T}}$, which includes the convective derivative, pressure and viscous terms, has components

$$Q_u(u, v, w, p) = \frac{\partial(uu)}{\partial x} + \frac{1}{r}\frac{\partial(rvu)}{\partial r} + \frac{1}{r}\frac{\partial(wu)}{\partial \theta} + \frac{\partial p}{\partial x} - \frac{1}{\mathrm{Re}}\left[\frac{\partial^2 u}{\partial x^2} + \frac{1}{r}\frac{\partial}{\partial r}\left(r\frac{\partial u}{\partial r}\right) + \frac{1}{r^2}\frac{\partial^2 u}{\partial \theta^2}\right], \tag{2}$$

$$Q_v(u, v, w, p) = \frac{\partial(uv)}{\partial x} + \frac{1}{r}\frac{\partial(rvv)}{\partial r} + \frac{1}{r}\frac{\partial(wv)}{\partial \theta} - \frac{w^2}{r} + \frac{\partial p}{\partial r} - \frac{1}{\mathrm{Re}}\left[\frac{\partial^2 v}{\partial x^2} + \frac{1}{r}\frac{\partial}{\partial r}\left(r\frac{\partial v}{\partial r}\right) + \frac{1}{r^2}\frac{\partial^2 v}{\partial \theta^2} - \frac{2}{r^2}\frac{\partial w}{\partial \theta} - \frac{v}{r^2}\right], \tag{3}$$

$$Q_w(u, v, w, p) = \frac{\partial(uw)}{\partial x} + \frac{1}{r}\frac{\partial(rvw)}{\partial r} + \frac{1}{r}\frac{\partial(ww)}{\partial \theta} + \frac{vw}{r} + \frac{1}{r}\frac{\partial p}{\partial \theta} - \frac{1}{\mathrm{Re}}\left[\frac{\partial^2 w}{\partial x^2} + \frac{1}{r}\frac{\partial}{\partial r}\left(r\frac{\partial w}{\partial r}\right) + \frac{1}{r^2}\frac{\partial^2 w}{\partial \theta^2} + \frac{2}{r^2}\frac{\partial v}{\partial \theta} - \frac{w}{r^2}\right]. \tag{4}$$

The above equations are written in dimensionless form, with Re denoting the Reynolds number in terms of a characteristic length and velocity. Here $u$, $v$ and $w$ represent the nondimensional velocity components in the axial, radial, and circumferential directions, respectively, while $t$, $x$ and $r$ are nondimensional time and space coordinates (see Fig. 1), using the annular clearance $h$ and the mean flow velocity $U_o$ as appropriate length and velocity scales (see Fig. 1); thus,

$$\begin{gathered} x = x^*/h, \quad r = r^*/h, \quad t = t^* U_o/h, \quad \omega = \omega^* h/U_o, \\ u = u^*/U_o, \quad v = v^*/U_o, \quad w = w^*/U_o, \quad \mathbf{V} = \mathbf{V}^*/U_o, \\ p = (p^* - p^*_\infty)/(\rho^* U_o^2), \quad \mathrm{Re} = hU_o/\nu = \tfrac{1}{2}\mathrm{Re}_{D_h}, \quad l = l^*/h, \end{gathered} \tag{5}$$

where the asterisk denotes the dimensional quantities, and $\mathrm{Re}_{D_h}$ is the Reynolds number based on the hydraulic diameter of the annulus ($D_h = 2h$). For the case of quiescent fluid, the pressure as well as the velocities, time and frequency are nondimensionalized using $U_o = \omega^* h$ as the flow velocity scale.

The numerical solution of Eq. (1) is obtained by using a three-point backward implicit scheme for the real time discretization

$$\frac{3\mathbf{V}^{n+1} - 4\mathbf{V}^n + \mathbf{V}^{n-1}}{2\Delta t} + \mathbf{Q}^{n+1} = \mathbf{0}, \tag{6}$$

where $\Delta t = t^{n+1} - t^n = t^n - t^{n-1}$ is real time step and $\mathbf{Q}^{n+1} = \mathbf{Q}(\mathbf{V}^{n+1}, p^{n+1})$.

The unsteady flow solution is known (assumed) at time levels $t^{n-1}$ and $t^n$, and the solution at time level $t^{n+1}$ has to be obtained from the equations

$$\mathbf{V}^{n+1} + \alpha\mathbf{Q}^{n+1} = \boldsymbol{F}^n, \quad \boldsymbol{\nabla}\cdot\mathbf{V}^{n+1} = 0, \tag{7,8}$$

where $\alpha = \frac{2}{3}\Delta t$, $\mathbf{F}^n = \frac{1}{3}(4\mathbf{V}^n - \mathbf{V}^{n-1})$.

In the unsteady flow problem associated with forced vibration, the known velocity $\mathbf{V}_B^{n+1}$ of the moving boundary is imposed as a boundary condition, and the velocity at the fixed solid boundary is zero due to no-slip condition; thus Eqs. (7) and (8) are subjected to the following boundary conditions (see Fig. 1):

$$u = u_B = 0, \quad v = v_B = \dot{e}\cos\theta, \quad w = w_B = -\dot{e}\sin\theta, \tag{9}$$

where $he(t) = -h\varepsilon\cos\omega t$, $\dot{e} = \mathrm{d}e/dt$, and the subscript $B$ indicates "on the wall of the structure". If rocking motion of the outer cylinder is considered, as shown in Fig. 4(b), then the following boundary condition is applied:

$$e(t, x) = -\frac{e(t)}{l_2}x + \frac{e(t)(l_1 + l_2)}{l_2}. \tag{10}$$

At the inlet of the annular passage ($x = -l_0$), the in-flow boundary conditions are defined by the nondimensional velocity components of fully developed laminar flow:

$$u = \frac{U^*(r^*)}{U_o} = 2\frac{(r_0^2 - r_i^2)\ln(r/r_i) - (r^2 - r_i^2)\ln(r_0/r_i)}{(r_0^2 + r_i^2)\ln(r_0/r_i) - (r_0^2 - r_i^2)}, \quad v = w = 0. \tag{11}$$

The spatial discretization uses central differencing based on a staggered (Harlow and Welch, 1965), stretched (Vinokur, 1983) grid, see Fig. 6; hence, there is no need for the pressure to be defined at the fixed or moving boundaries, and also more grid points are concentrated near these boundaries.

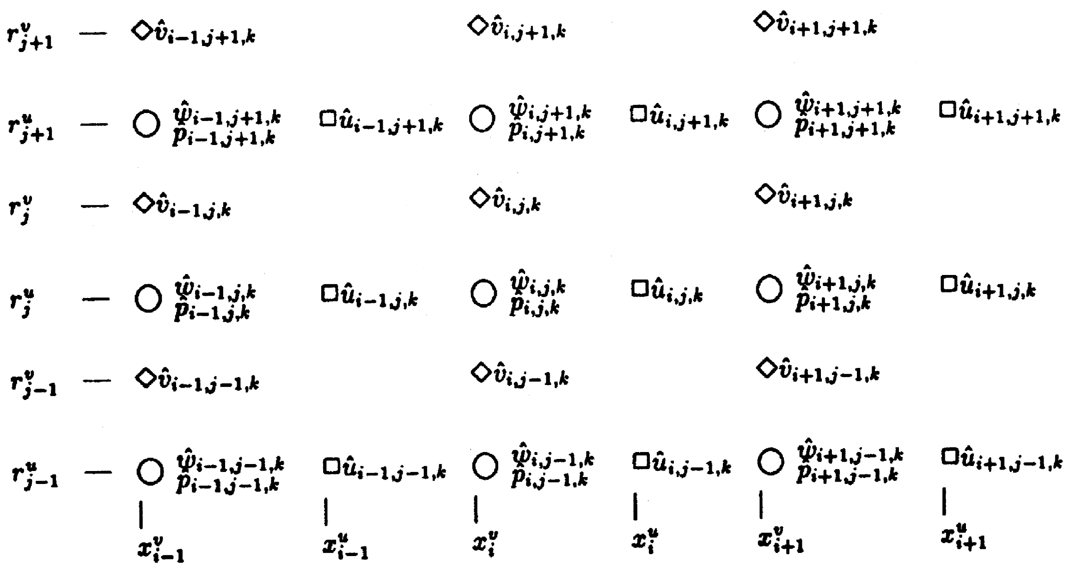

Fig. 6. Schematic representation of the staggered grid used in the spatial discretization of the three-dimensional nonlinear equations.

The solution of Eqs. (7) and (8) is obtained by using an iterative pseudo-time relaxation method with artificial compressibility (Soh and Goodrich, 1988), by which the equations are replaced by

$$\frac{\partial \check{\mathbf{V}}}{\partial \tau} + \check{\mathbf{V}} + \alpha \check{\mathbf{Q}} = \mathbf{F}^n, \quad \delta\left(\frac{\partial \check{p}}{\partial \tau}\right) + \nabla \cdot \check{\mathbf{V}} = 0, \tag{12,13}$$

where $\check{\mathbf{V}}(\tau)$ and $\check{p}(\tau)$ are the intermediate values of the velocity and pressure between real-time levels $t^n$ and $t^{n+1}$. Here, $\tau$ is the pseudo-time variable, and $\delta$ represents an artificially added compressibility which can be based on a simplified theory of characteristics (Chorin, 1967; Soh, 1987).

An implicit Euler scheme is used to semidiscretize in pseudo-time Eqs. (12) and (13) in the form

$$\frac{\check{\mathbf{V}}^{\nu+1} - \check{\mathbf{V}}^{\nu}}{\Delta\tau} + \check{\mathbf{V}}^{\nu+1} + \alpha \check{\mathbf{Q}}^{\nu+1} = \mathbf{F}^n, \quad \frac{\check{p}^{\nu+1} - \check{p}^{\nu}}{\Delta\tau} + \frac{1}{\delta} \nabla \cdot \check{\mathbf{V}}^{\nu+1} = 0, \tag{14,15}$$

with the initial values of $\check{\mathbf{V}}^1 = \mathbf{V}^n$ and $\check{p}^1 = p^n$. The resulting pseudo-time equations are recast in terms of pseudo-time variations $\Delta\mathbf{V} = \check{\mathbf{V}}^{\nu+1} - \check{\mathbf{V}}^{\nu}$, $\Delta\mathbf{Q} = \check{\mathbf{Q}}^{\nu+1} - \check{\mathbf{Q}}^{\nu}$ and $\Delta p = \check{p}^{\nu+1} - \check{p}^{\nu}$. Thus, Eqs. (14) and (15) can be recast in delta form as

$$(1 + \Delta\tau)\Delta\mathbf{V} + \alpha\Delta\tau\Delta\mathbf{Q} = \Delta\tau(\mathbf{F}^n - \check{\mathbf{V}}^{\nu} - \alpha\check{\mathbf{Q}}^{\nu}), \tag{16}$$

$$\Delta p + \frac{\Delta\tau}{\delta} \nabla \cdot (\Delta\mathbf{V}) = -\frac{\Delta\tau}{\delta} \nabla \cdot \check{\mathbf{V}}^{\nu}, \tag{17}$$

where $\Delta\mathbf{V} = [\Delta u, \Delta v, \Delta w]^{\mathrm{T}}$ and $\Delta\mathbf{Q} = [\Delta Q_u, \Delta Q_v, \Delta Q_w]^{\mathrm{T}}$ in which $\Delta Q_u$, $\Delta Q_v$ and $\Delta Q_w$ are expressed, using lagged nonlinearities in which the values of $\check{u}^{\nu}$, $\check{v}^{\nu}$ and $\check{w}^{\nu}$ are known at previous time levels and $\Delta u$, $\Delta v$ and $\Delta w$ are unknown in the $\Delta\mathbf{Q}$ components; for example,

$$\Delta Q_u = \frac{\partial(\check{u}^{\nu}\Delta u)}{\partial x} + \frac{1}{r}\frac{\partial(r\check{v}^{\nu}\Delta u)}{\partial r} + \frac{1}{r}\frac{\partial(\check{w}^{\nu}\Delta u)}{\partial \theta} + \frac{\partial(\Delta p)}{\partial x} - \frac{1}{\mathrm{Re}}\left[\frac{\partial^2(\Delta u)}{\partial x^2} + \frac{1}{r}\frac{\partial}{\partial r}\left(r\frac{\partial(\Delta u)}{\partial r}\right) + \frac{1}{r^2}\frac{\partial^2(\Delta u)}{\partial \theta^2}\right]. \tag{18}$$

A factored ADI scheme (Soh, 1987) is used in this analysis to separate the numerical integration of Eqs. (16) and (17) in $x$, $r$ and $\theta$ sweeps, which reads

$$(\mathbf{I} + \alpha\Delta\tau\mathbf{D}_x)(\mathbf{I} + \alpha\Delta\tau\mathbf{D}_r)(\mathbf{I} + \alpha\Delta\tau\mathbf{D}_\theta)\Delta\mathbf{f} = \Delta\tau\mathbf{R}, \tag{19}$$

where $\Delta\mathbf{f} = [\Delta u, \Delta v, \Delta w, \Delta p]^{\mathrm{T}}$, and $\mathbf{I}$ represents the unit matrix.

Eq. (19) can be recast in delta form:

$$(\mathbf{I} + \alpha\Delta\tau\mathbf{D}_x)\Delta\tilde{\mathbf{f}} = \Delta\tau\mathbf{R}, \quad (\mathbf{I} + \alpha\Delta\tau\mathbf{D}_r)\Delta\bar{\mathbf{f}} = \Delta\tilde{\mathbf{f}}, \quad ((\mathbf{I} + \alpha\Delta\tau\mathbf{D}_\theta)\Delta\mathbf{f} = \Delta\bar{\mathbf{f}}, \tag{20}$$

where the matrices $\mathbf{D}_x$, $\mathbf{D}_r$ and $\mathbf{D}_\theta$ are given by

$$\mathbf{D}_x = \begin{bmatrix} L+1/\alpha & 0 & 0 & \partial/\partial x \\ 0 & L & 0 & 0 \\ 0 & 0 & L & 0 \\ 1/(\alpha\delta)\partial/\partial x & 0 & 0 & 0 \end{bmatrix}, \tag{21}$$

$$\mathbf{D}_r = \begin{bmatrix} M & 0 & 0 & 0 \\ 0 & M+1/\alpha+1/(\mathrm{Re}\,r^2) & -\breve{w}^v/r & \partial/\partial r \\ 0 & 0 & M+\breve{v}^v/r+1/(\mathrm{Re}\,r^2) & 0 \\ 0 & (1/\alpha\delta)(\partial/\partial r)(r) & 0 & 0 \end{bmatrix}, \tag{22}$$

$$\mathbf{D}_\theta = \begin{bmatrix} N & 0 & 0 & 0 \\ 0 & N & (2/\mathrm{Re}\,r^2)\partial/\partial\theta & 0 \\ 0 & -(2/\mathrm{Re}\,r^2)\partial/\partial\theta & N+1/\alpha & (1/r)\partial/\partial\theta \\ 1/(\alpha\delta)\partial/\partial x & 0 & (1/\alpha\delta r)\partial/\partial\theta & 0 \end{bmatrix} \tag{23}$$

in which

$$L\varphi = \frac{\partial(\breve{u}^v\varphi)}{\partial x} - \frac{1}{\mathrm{Re}}\frac{\partial^2\varphi}{\partial x^2}, \quad M\varphi = \frac{\partial(r\breve{v}^v\varphi)}{r\partial r} - \frac{1}{\mathrm{Re}}\frac{\partial}{r\partial r}\left(r\frac{\partial\varphi}{\partial r}\right), \quad N\varphi = \frac{\partial(\breve{w}^v\varphi)}{r\partial\theta} - \frac{1}{\mathrm{Re}}\frac{\partial^2\varphi}{r^2\partial\theta^2},$$

$$\mathbf{R} = \begin{bmatrix} F_u^n - \breve{u}^v - \alpha\breve{Q}_u^v \\ F_v^n - \breve{v}^v - \alpha\breve{Q}_v^v \\ F_w^n - \breve{w}^v - \alpha\breve{Q}_w^v \\ -(1/\delta)\nabla\cdot\breve{\mathbf{V}}^v \end{bmatrix},$$

where $\varphi$ is a dummy variable representing $u$, $v$ or $w$.

Eqs. (20) is further spatially discretized by central differencing, as mentioned before, on a stretched staggered grid based on hyperbolic stretching functions to concentrate more points near the oscillating and fixed boundaries (Section 3.2). The final computational results at each real time step are $\Delta u$, $\Delta v$, $\Delta w$ and $\Delta p$ from which the values of unsteady $u$, $v$, $w$ and $p$ at time $n+1$ are obtained via

$$u^{n+1} = u^n + \Delta u, \quad v^{n+1} = v^n + \Delta v, \quad w^{n+1} = w^n + \Delta w, \quad p^{n+1} = p^n + \Delta p;$$

they are the output of the numerical computation. It should be mentioned that the values obtained for these quantities are steady plus complex unsteady values. First, by using a sort of FFT programme (Cooley et al., 1969), the amplitude and phase angle of each variable is determined and then the steady part is subtracted from the calculated value to obtain the unsteady part.

The values of $\delta$ and $\Delta\tau$ are determined in the manner proposed by Soh and Goodrich (1988). The real time step is chosen as $\Delta t = 2\pi/(19\omega_n)$, which is less than $\Delta t = 2\pi/(10\omega_n)$ recommended in the literature. For more details refer to Mekanik (1994).

### 3.2. Implementation

A satisfactory grid generation and grid point distribution are major requirements for the numerical solution to be accomplished successfully in terms of accuracy and stability. While the grids are staggered, the distribution functions used for grid point location are a hyperbolic tangent stretching function for the radial direction $r$ and a hyperbolic sine stretching function in the axial direction $x$ (Vinokur, 1983; Thompson et al., 1985), with coordinate $\theta$, $0 \leqslant \theta \leqslant \pi$, uniformly distributed along the circumferential direction. A typical staggered grid point distribution in 3-D is shown in Fig. 6, and in general form in the physical domain and in stretched form in the computational domain in Fig. 7.

To solve the Navier–Stokes and continuity equations in the 3-D annular configuration, we need to generate a 3-D mesh. This is done by choosing appropriate inner and outer radii, the stretching functions, and the number of grid

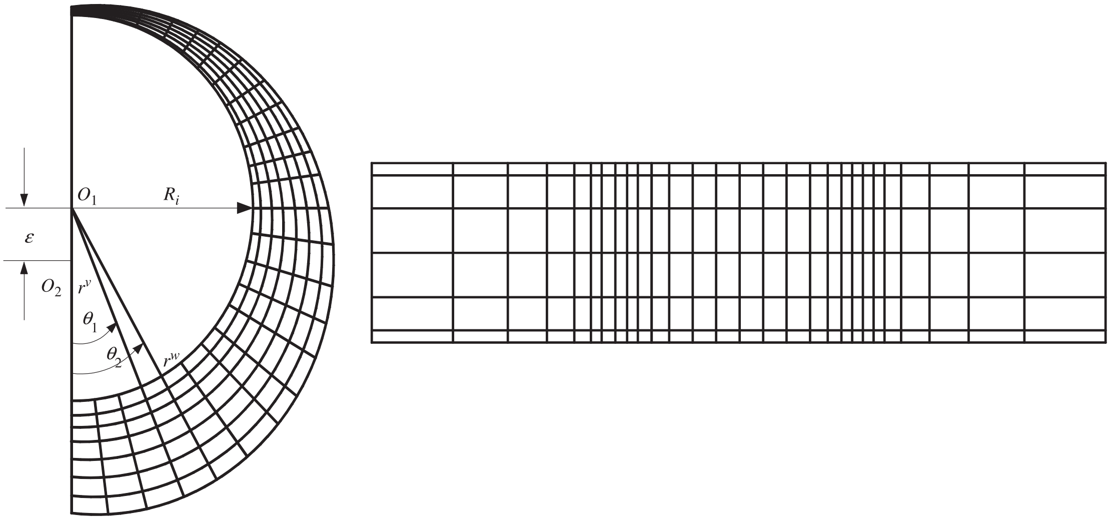

Fig. 7. Physical and computational domains using the stretched grids.

points in the $r$-, $x$- and $\theta$-directions; for this purpose, the numerical computations have been performed on a nondimensional mesh with inner radius $r_i = 4.785$ and outer radius $r_o = 5.785$ with $89 \times 12 \times 15$ grid points in those directions.

The boundary conditions imposed on the equations to be solved are such that all perturbations in the flow quantities be equal to zero at both inlet and outlet of the domain, including velocity components and pressure. The initial conditions for the perturbations are set equal to zero before starting the vibration of the outer cylinder, and the integration of the equations is implemented until a periodic solution is achieved, which takes at least three harmonic cycles.

To get the 3-D solution we must first have a steady solution for the flow in the annular space before getting into the solution procedure of the unsteady problem. Therefore, the problem is first solved for the steady case using the velocity profile of Eq. (11). Then, using the steady results, the unsteady solution is started. As seen in the equations of Section 3.1, a Reynolds number needs to be specified, even when the flow velocity is zero (quiescent fluid). In such cases, we use the oscillatory Reynolds number, or Stokes number, $\mathrm{S} = \omega^* h^2/\nu$, for oscillation at dimensional frequency $\omega^*$. For $U \neq 0$, since $\omega = \omega^* h/U_o$, we can express $\mathrm{Re}_{D_h} = 2\mathrm{S}/\omega$. The computation can be done for different Reynolds and Stokes numbers, always in the laminar regime.

For all of the results obtained in this research, the time step $\Delta t = T/N$ with $N = 19$ was used; the compressibility factor $\delta$ and pseudo-time step $\Delta\tau$ were chosen based on the criteria supplied by Chorin (1967) and Soh and Goodrich (1988), and finally implementing numerical experiments by correcting the values of $\delta$ and $\Delta\tau$ via appropriate correction factors and the Courant number in the range of 30–40. In all computations, convergence was reached and the iterations were stopped in pseudo-time when the r.m.s. values of the numerical residuals of the momentum and continuity equations were all less than $10^{-4}$, which is low enough to ensure that the governing equations of fluid motion are satisfied for each real-time step. Samples of the numerical results obtained are discussed in Section 5, and later on they are compared with the experimental results.

## 4. Experimental results

The experimental results in Figs. 8–12 have been obtained for transverse translational and rocking motions of the outer cylinder. These figures represent sample data, chosen out of 1000 files of experimental data obtained. Normally, in the figures shown, the panels on the left are for no fluid flow and those on the right for fluid flow with $\mathrm{Re}_{D_h} = 2900$, unless otherwise indicated. The figures present the following data: (i) the amplitude spectrum of the unsteady pressure for specific transducers; (ii) the unsteady pressure versus distance along the cylinder, obtained by all pressure transducers; (iii) the phase angle versus the distance along the cylinder, obtained by all pressure transducers; (iv) the coherence spectrum of the unsteady pressure with respect to the acceleration of the outer cylinder for specific pressure transducers.

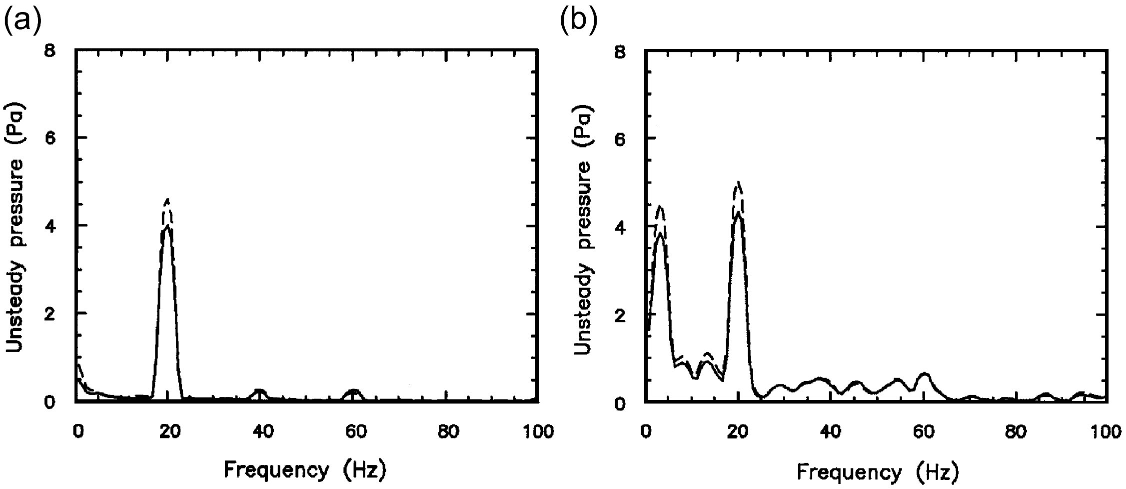

Fig. 8. Samples of the unsteady pressure spectra in the annulus, as measured by pressure transducers on the inner annular wall while the outer wall (cylinder) was in translational motion, for $\varepsilon = 0.1075$ and $f = 20$ Hz: ———, pressure transducer 1 (see Fig. 4); – – –, pressure transducer 2. (a) No flow; (b) $\mathrm{Re}_{D_h} = 2900$.

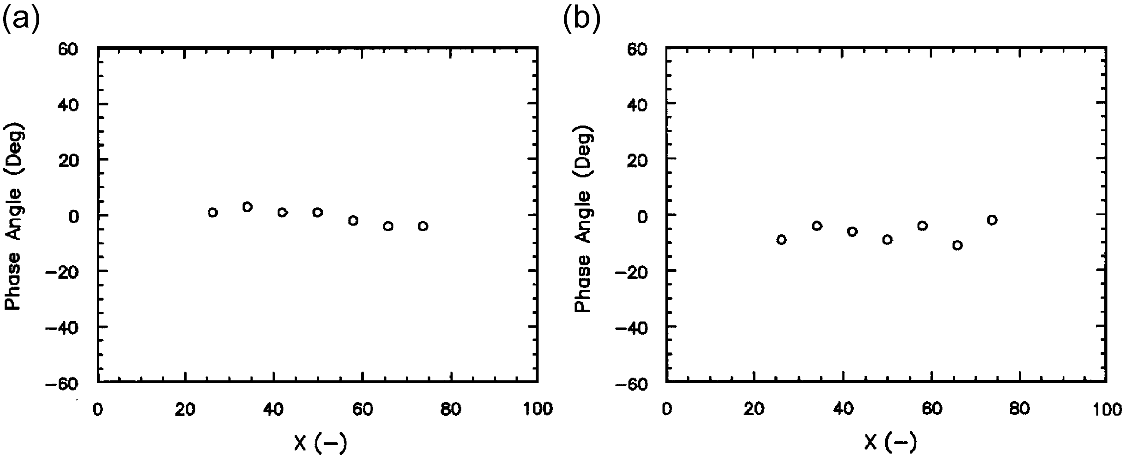

Fig. 9. Samples of phase angles of the unsteady pressure with respect to the displacement of the outer cylinder in translational motion from pressure transducers 1 to 7 shown in Fig. 4(a) for $\varepsilon = 0.1075$ and $f = 20$ Hz. $X$ is defined as $x/h$. (a) No flow; (b) $\mathrm{Re}_{D_h} = 2900$.

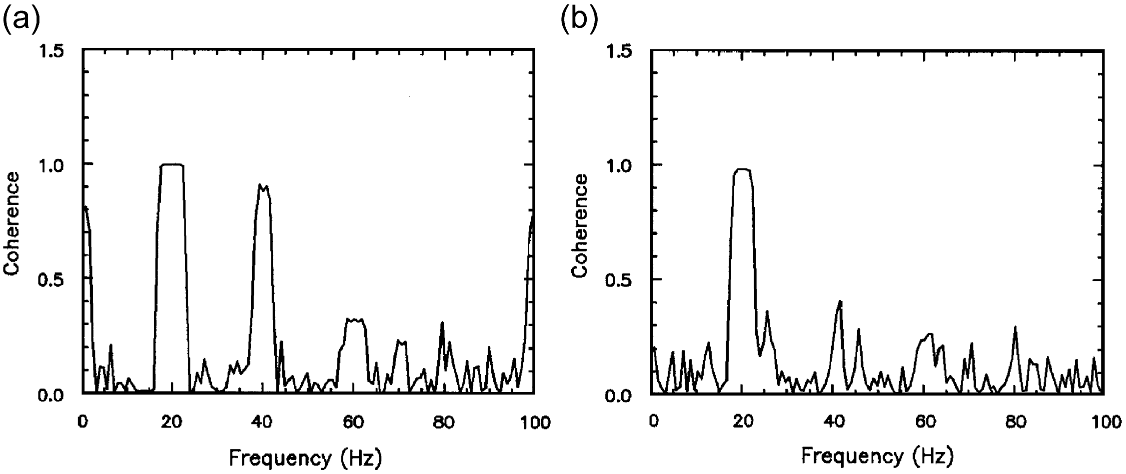

Fig. 10. Samples of coherence spectra of the unsteady pressure with respect to the acceleration of the outer cylinder in translational motion from pressure transducer 3 (see Fig. 4(a)); $\varepsilon = 0.1075$ and $f = 20$ Hz. (a) No flow; (b) $\mathrm{Re}_{D_h} = 2900$.

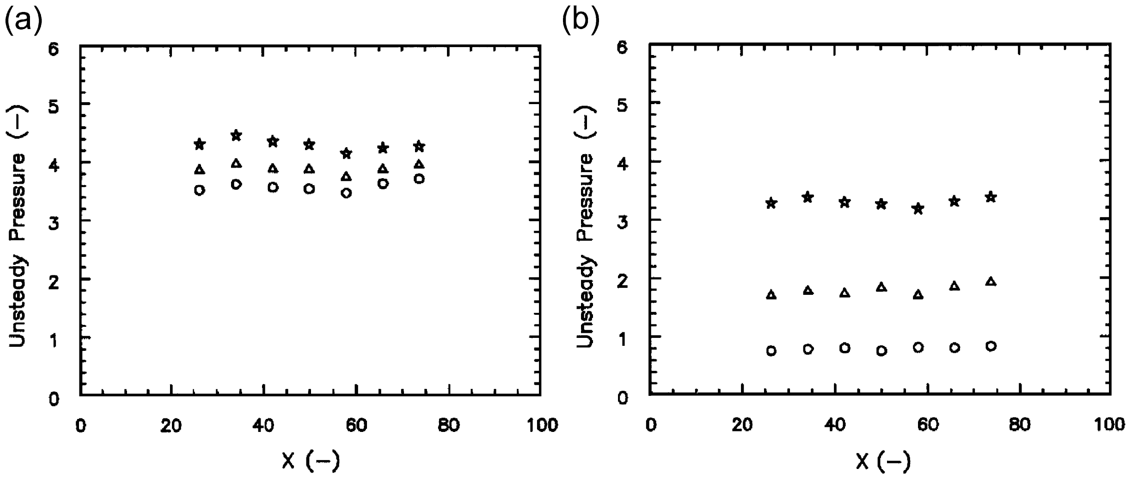

Fig. 11. Nondimensional unsteady pressure versus length for translational motion of the outer cylinder from pressure transducers 1 to 7 shown in Fig. 4(a). The amplitude is $\varepsilon = 0.1075$and the frequencies are: ○, $f = 20$ Hz; △, $f = 30.4$ Hz; *, $f = 40$ Hz. (a) No flow; (b) $\mathrm{Re}_{D_h} = 2900$.

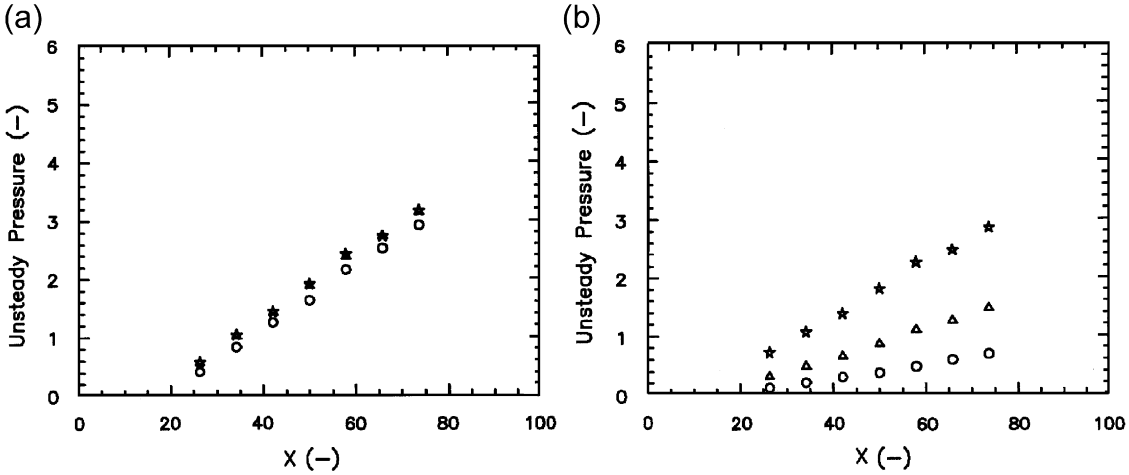

Fig. 12. Nondimensional unsteady pressure versus length for rocking motion of the outer cylinder from pressure transducers 1 to 7 shown in Fig. 4(b). The amplitude is $\varepsilon = 0.1075$and the frequencies are: ○, $f = 20$ Hz; △, $f = 30.4$ Hz; *, $f = 40$ Hz. (a) No flow; (b) $\mathrm{Re}_{D_h} = 2900$.

Fig. 8 presents the unsteady pressure amplitude readings for translational motion of the cylinder for $\varepsilon = 0.1075$ and $f = 20$ Hz, measured by individual pressure transducers through the spectrum analyzer, recorded and processed by the computer[1]; $\varepsilon$ is the amplitude of oscillation of the outer cylinder divided by the annular gap, $h$. Fig. 9 presents the phase angles along the axis of the centre-body measured by pressure transducers 1–7 (see Fig. 4(a)), again for $\varepsilon = 0.1075$ and $f = 20$ Hz, and translational motion. From this figure it is clear that the phase angles are nonzero but close to zero, which is reasonable because the fluid is air. Fig. 10 presents the coherence between the unsteady pressure signals from pressure transducer 3 in Fig. 4(a) and the acceleration signals, for the same $\varepsilon$ and $f$, and type of motion.

---

[1] The origin of the lower frequency peak ($f \approx 3$ Hz) in Fig. 8(b) is probably mechanical or flow-related upstream vibration, transmitted via the flowing fluid. Such peaks are smaller, as compared to the main one at the excitation frequency, for higher frequencies: $f = 30$, 40 and 50 Hz; they are not present at all at $f < 20$ Hz. During the experiments, there were certain devices used to reduce the effects of non-uniformity in the flow and the noise coming from the surroundings. These devices are honeycombs at the entrance and exit of the annulus, as shown in Fig. 2, and an acoustic filter and a noise-attenuation plenum chamber, not shown in the figure.

The same types of measurements as those shown in Figs. 8–10 have been obtained for rocking motion of the outer cylinder but are not presented here.

The results in Fig. 8 were obtained by using a nominal calibration factor for all the pressure transducers (0.07 mV/Pa, given in the transducer catalogue); whereas, as stated in Section 2.2, the true calibration factors varied from one transducer to the next. Thus, in a sense, these are raw data, shown only to illustrate the type and form of the data collected; hence, the unsteady pressure amplitudes for transducer 1 and 2 in Fig. 8 should not be compared to each other. This has to be done later, once the results have been corrected with the pertinent calibration factors for each transducer.

These corrected results, the unsteady pressure amplitudes—for all the transducers—for both translational and rocking motions are presented in Figs. 11 and 12, for $\varepsilon = 0.1075$ and $f = 20$, 30.4 and 40 Hz plotted against $X$ (i.e., along the annular passage), and the phase angle for $\varepsilon = 0.1075$ and $f = 20$ Hz are shown in Fig. 9, also plotted against $X$.

It is seen in Fig. 11 (for translational motion) that there are small variations of the measured pressure with $X$, while ideally there should be none for translational motion; these variations are nevertheless acceptably small. It is clearly seen that the amplitude of the unsteady pressure increases with frequency, both with and without flow. Interestingly, and perhaps counterintuitively, the unsteady pressure is rather lower in the case of a flowing fluid (see explanation given in the next paragraph).

In Fig. 12 (for rocking motion) the uniformity of the pressure readings with respect to the frequency of oscillation is much better than those of Fig. 11; a plausible reason for this is proposed in Section 6. For the rocking motion the hinge is located at $X = x/H = 15.5$ from the right-hand side of the outer cylinder; see Fig 4(b). If we consider the forced vibration as a source of energy input into the system with the energy of the cylinder given by $\frac{1}{2}M(\omega\varepsilon)^2$, this energy must be dissipated by the cylinder or absorbed by the fluid. Since the energy input is sustained by the velocity of the boundary, $\omega\varepsilon$, it must be absorbed by the fluid and converted into potential energy. The increase in the pressure of the fluid is the result of this energy input. Thus, when we have quiescent fluid, the energy input is constant because $\omega = 1$ and $\varepsilon = 0.05375$. Therefore, the pressure amplitude is constant as shown in Figs. 11(a) and 12(a). When we have fluid flow, the energy input is frequency dependent, i.e., for $\mathrm{Re} = 2900$ and $f = 20$, 30.4, 40 Hz, $\omega = 0.462$, 0.702 and 0.924, respectively. With constant $\varepsilon = 0.05375$ and the variable $\omega$ as above, the energy input and consequently the pressure becomes a function of the frequency, as shown in Figs. 11(b) and 12(b). These effects can also be seen in Fig. 13. There are substantial disturbances introduced in the annular space during the motion of the cylinder due to the fluid flow with $\mathrm{Re}_{D_h} = 2900$ (compare Fig. 8(a) and 8(b)). The measured coherences (Fig. 10) indicate that the unsteady pressure was generated mostly by the oscillation of the outer cylinder (e.g., the magnitudes of the coherence readings approach unity); i.e., the other extraneous factors have less effect on the magnitude of the measured pressure signals. The coherence plots show several peaks corresponding to the higher harmonics which cannot be easily seen in the pressure spectra.

Errors will creep into all experiments, regardless of how much care is exerted. To ascertain the accuracy of the experimental results, an error analysis was conducted. In this experimental investigation, the types of errors vary; they include the apparatus, instrument errors, systematic errors, random errors, precision errors, errors coming from disturbances, etc. Some measures were taken in these experiments to reduce some of these errors. The data obtained in this experimental investigation are, to some extent, single-reading data rather than multiple-reading data; although some of the measurements were repeated several times. Based on a theoretical error analysis and considering the precision in the apparatus and accuracy in measuring devices, the maximum error in the pressure measurements was estimated to be $\pm 0.25-0.29$ Pa, which is less than 10% of the pressure readings. The uncertainties in the phase angles are $\pm 5°$ for all phase angle measurements. The uncertainty pertinent to the flow velocity measurements for a specific orifice plate and manometer reading were 2–3% approximately.

## 5. Theoretical results

Fig. 13 presents unsteady pressure amplitudes at different frequencies and different amplitudes subjected to translational oscillation of the outer cylinder, both for no flow and with flow. The results obtained are for small-amplitude oscillation; i.e., for narrow annular gaps, the amplitudes are in the range $\varepsilon \leqslant 0.2$.

For uniform annular space with the outer cylinder in rocking motion, Fig. 14 presents the unsteady pressure and phase angle for quiescent fluid at $\omega = 1.0$ corresponding to $f = 20$ Hz and $\varepsilon = 0.1075$, and for fluid flow with $\mathrm{Re}_{D_h} = 2900$, $\omega = 0.462$ corresponding to $f = 20$ Hz[2] and $\varepsilon = 0.1075$.

---

[2] As explained in Section 3.2, for quiescent fluid, ($U_o = 0$, we replace the Reynolds number with Stokes number in the numerical calculations. Thus, in this case, $\omega = 1$ for all frequencies of oscillation, including $f = 20$ Hz. But for fluid flow, since $\mathrm{Re}_{D_h} = 2U_o h/\nu$ and $\mathrm{S} = \omega^* h^2/\nu$, for $f = 20$ Hz, $\nu = 1.62 \times 10^{-5}\,\mathrm{m}^2/\mathrm{s}$ and $h = 9.3 \times 10^{-3}$ mm, one obtains $\omega = 0.462$.

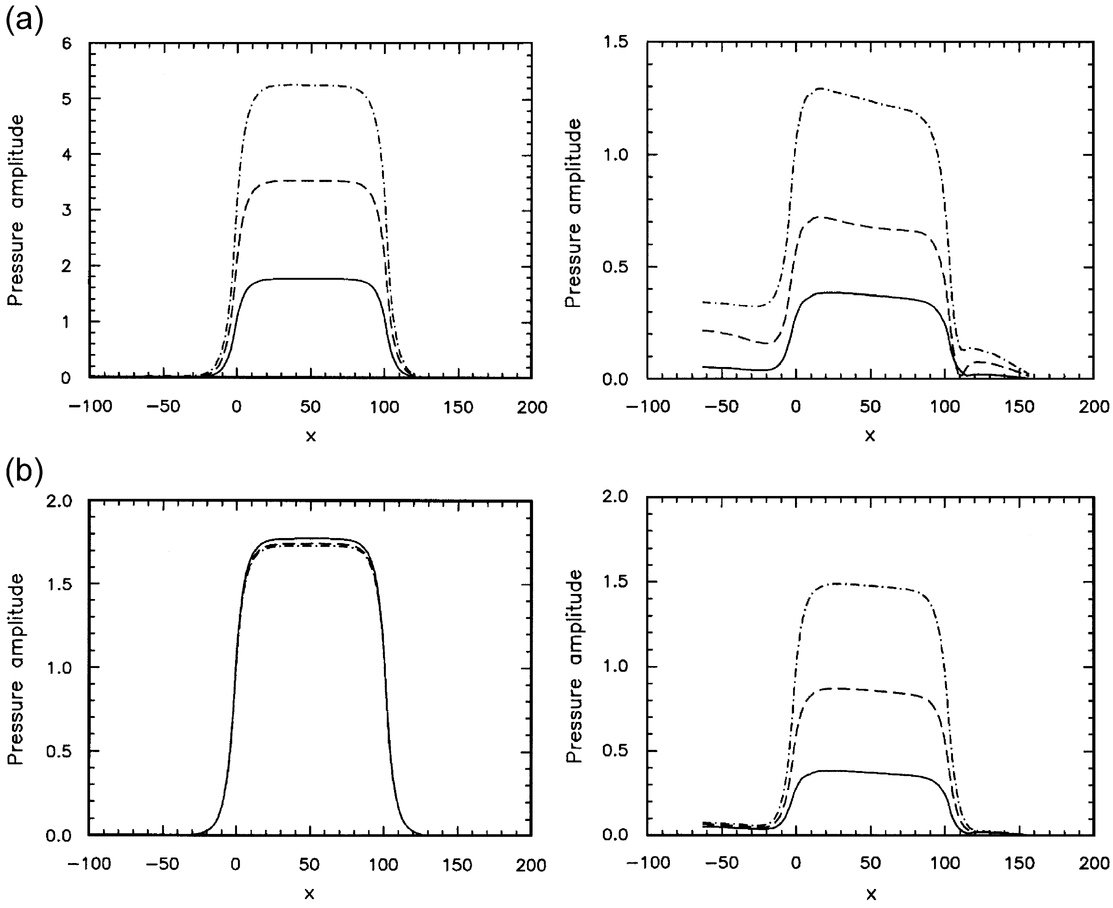

Fig. 13. Samples of the nondimensional unsteady pressure at different amplitudes and frequencies for translational motion of the outer cylinder. In (a): ———, $\varepsilon = 0.05375$; – – –, $\varepsilon = 0.1075$, –·–·–, $\varepsilon = 0.16125$ at $f = 20$ Hz. In (b): ———, $f = 20$ Hz; – – –, $f = 30.4$ Hz; –·–·–, $f = 40$ Hz at $\varepsilon = 0.05375$. Left-hand panels are for no flow and right-hand panels for $\mathrm{Re}_{D_h} = 2900$.

It is interesting to see that, for translational motion with quiescent fluid in the annulus, the pressure amplitude is perfectly flat in the oscillatory part of the annulus (left-hand panels of Fig. 13). For flowing fluid, however, as seen in the right-hand panels of Fig. 13, the amplitudes tend to drop a little downstream, the effect being most indicated at the larger amplitudes (notably for $\varepsilon = 0.16125$).

For rocking motion of the outer cylinder, the boundary conditions for the velocity on the vibrating wall are obtained using Eqs. (9) and (10). It is interesting to see (Fig. 14) that the unsteady pressure at the hinge location is in fact zero, indicating weak connection of the unsteady pressure along the annulus.

## 6. Comparison between experiment and theory

The final objective of this research is the comparison of the experimental results with the theoretical ones. In this regard, only samples of the comparison are presented.

Fig. 15 presents the comparison between the theoretical and experimental results for unsteady pressure and phase angle, in the case of translational motion of the cylinder. The agreement is good. In Fig. 15 (right-hand panels) the data are more scattered than those shown in left-hand panels; this is due to experimental errors and perhaps unsteadiness in the flow (see Section 4).

Fig. 16 presents a similar comparison between the theoretical and experimental results, but for rocking motion of the outer cylinder. It is seen that in this case the agreement between the two sets of results is excellent. The main reason for

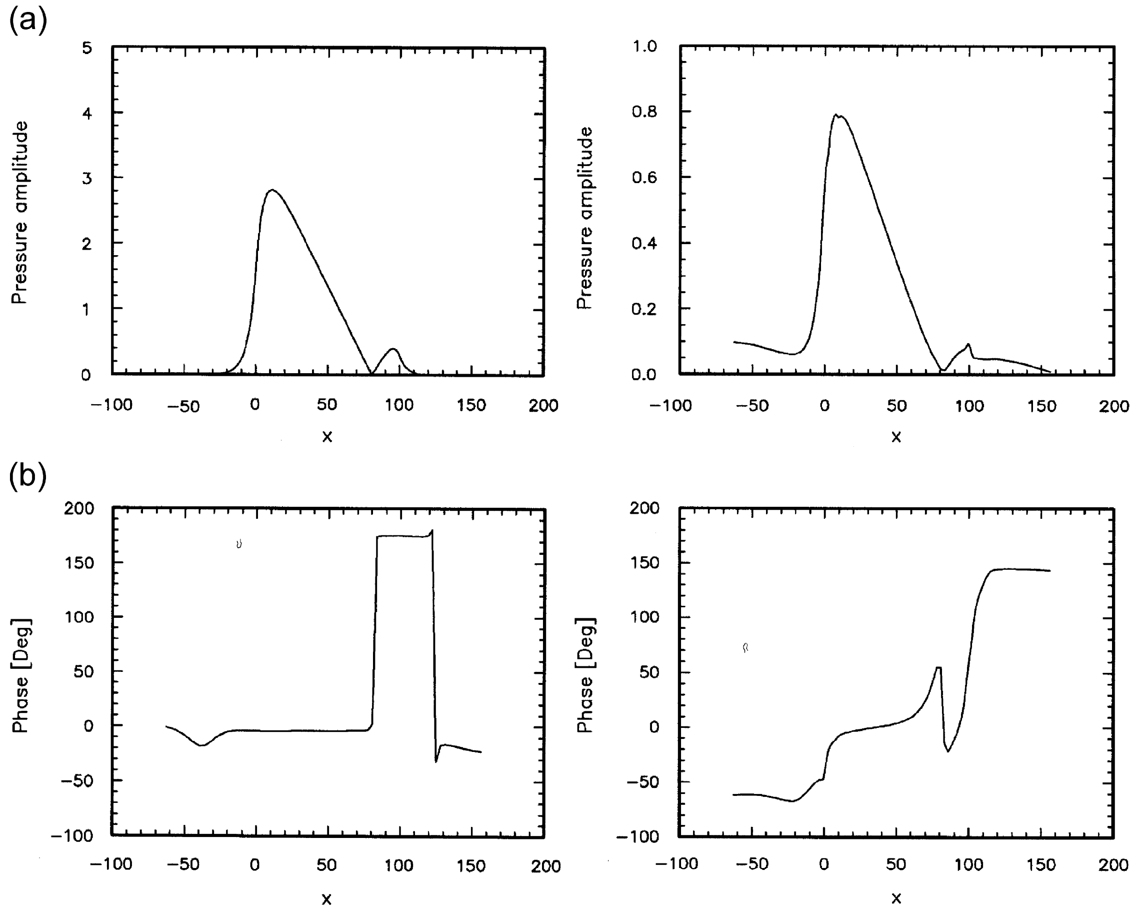

Fig. 14. (a) Sample of the nondimensional unsteady pressure amplitude and (b) phase angles during rocking motion of the outer cylinder at $\varepsilon = 0.1075$ and $f = 20\,\mathrm{Hz}$. Left-hand panels are for no flow and right-hand panels for $\mathrm{Re}_{D_h} = 2900$. Hinge location at $X = 81.0$.

this close agreement is that, for rocking motion of the outer cylinder, the moving cylinder is fixed at one end through the hinge, and its other end is supported by the shaker; thus the oscillation is constrained to be planar, much more than in the case of translational motion where small out-of-plane oscillation cannot be totally suppressed.

## 7. Conclusions

A comprehensive experimental study has been conducted for the purpose of validating an accurate numerical method. In the experiments, part of the outer cylindrical containment of the annular passage was put in oscillatory motion by a shaker, in either a translational or a rocking mode. The unsteady pressure all along the annular wall and the phase difference between the oscillation and the pressure were measured, either with quiescent fluid or with laminar air-flow in the annulus.

The pressure and phase were also calculated numerically, using a time-accurate integration method to solve the Navier–Stokes equations for the same annular geometry as in the experiments. In this method, a three-point backward implicit scheme in time was used to enhance the accuracy and efficiency of computation. The method used is based on artificial compressibility and pseudo-time integration. A factored ADI scheme was used to solve the scalar tridiagonal systems of equations obtained on stretched scattered grids.

The comparison between theoretical and experimental results shows that agreement between the two is generally very good, both in terms of the unsteady pressure amplitude along the annular passage and the corresponding phase difference with respect to the oscillation. In fact, in the case of rocking motion, when out-of-plane oscillation of the outer annular cylinder was minimized, agreement between theory and experiment is judged to be excellent.

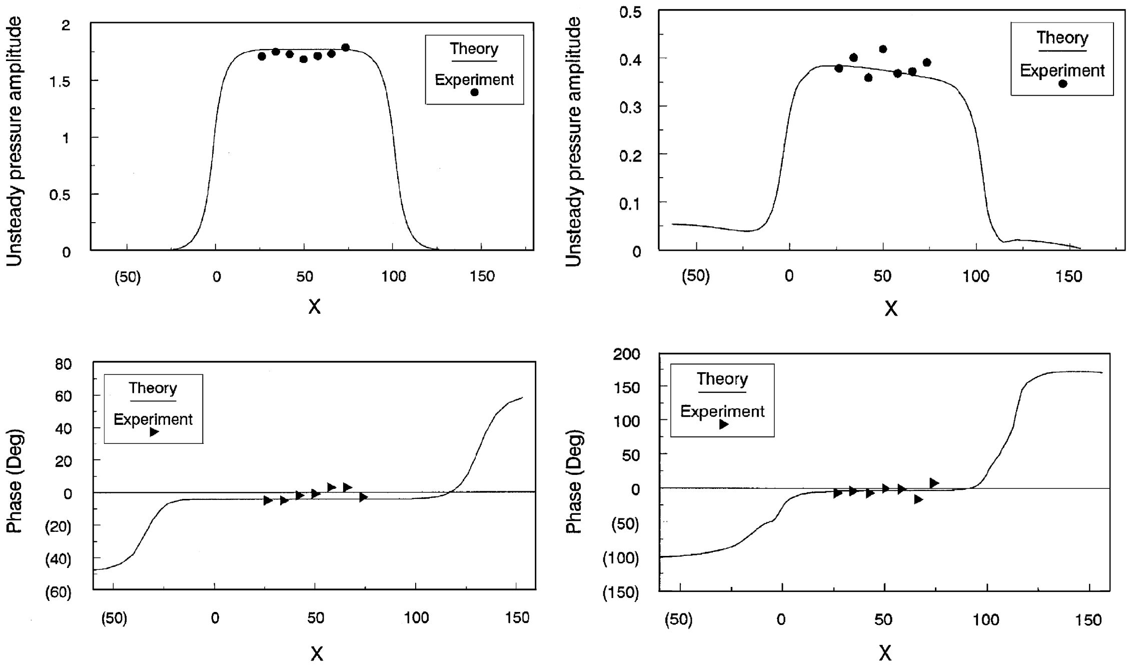

Fig. 15. Nondimensional unsteady pressure amplitude and phase angle with respect to the displacement of the outer cylinder in translational motion. Comparison between theoretical and experimental results for $\varepsilon = 0.1075$ and $f = 20\,\text{Hz}$. Left-hand panels are for no flow and right-hand panels for $\text{Re}_{D_h} = 2900$.

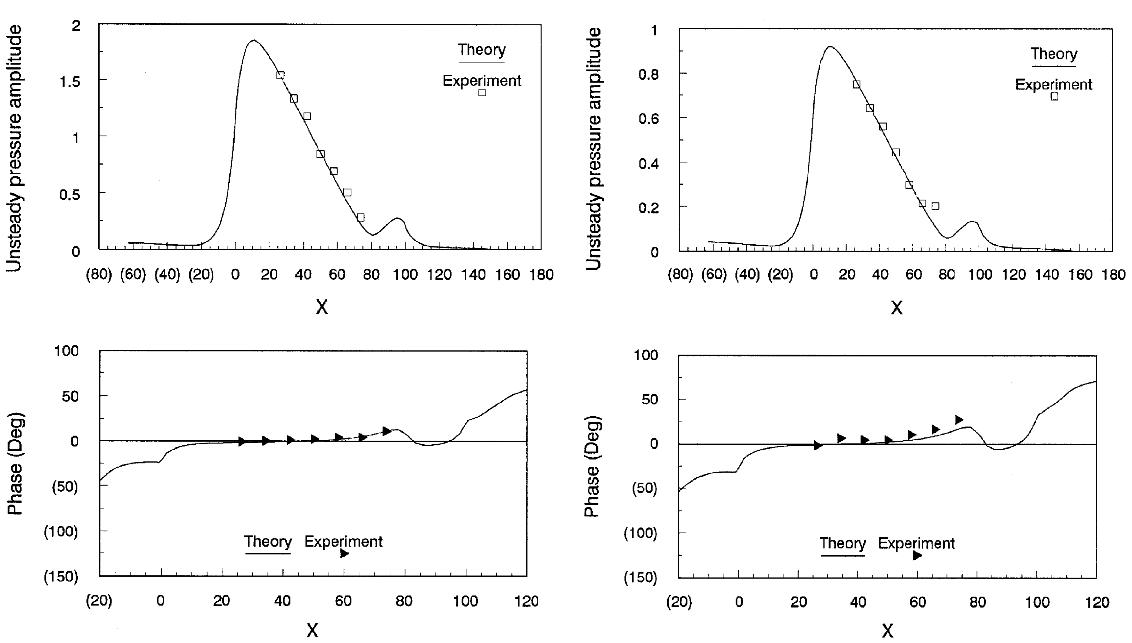

Fig. 16. Nondimensional unsteady pressure amplitude and phase angle with respect to the displacement of the outer cylinder in rocking motion. Comparison between theoretical and experimental results for $\varepsilon = 0.05375$ and $f = 30.4\,\text{Hz}$. Left-hand panels are for no flow and right-hand panels for $\text{Re}_{D_h} = 2900$.

In conclusion, this work has succeeded in validating the theoretical model, at least for values of $\varepsilon \leqslant 0.2$. It should be mentioned here that for $\varepsilon > 0.2$ it has been shown that the theory used in this paper becomes insufficiently accurate, as the boundary conditions must then be applied on the moving surface, rather than at its mean position; this requires either a moving solution grid or a time-dependent coordinate transformation, such as used, for example, in Mateescu et al. (1996). However, the present work can be used with confidence for flow-induced vibration and/or fluid–structure interaction analysis of annular and/or leakage flow problems.

## Acknowledgements

The support to this research by NSERC of Canada, FCAR of Québec and the Bu-Ali Sina University Research Center is gratefully acknowledged. The authors also acknowledge the contributions made by Professor D. Mateescu and François Bélanger, particularly in the development of the theoretical model.

## Appendix A

The Reynolds number is calculated from the following equations. To begin with, the flow rate is obtained from (Miller, 1989)

$$Q = 0.09970190\,\frac{C_d Y d^2}{\sqrt{1-\gamma^4}}\sqrt{\frac{h_w}{\rho_f}}, \tag{A.1}$$

where $Q$ is the volumetric flow rate of the air in ft$^3$/s, $Y$ is the air expansion factor for the orifice, taken to be $Y = 1$ for small differential pressure, $\gamma = d/D$, and $C_d$ is the coefficient of discharge for the orifice, given by

$$C_d = C_\infty + \frac{b}{\mathrm{Re}_D^n}$$

with $b = 91.71\gamma^{25}$, $n = 0.75$, $\mathrm{Re}_D = V_1 D/\nu$, $V_1$ being the velocity of air upstream of the orifice; $C_\infty$ is given by

$$C_\infty = 0.5959 + 0.0312\gamma^{2.1} - 0.184\gamma^8 + 0.39\frac{\gamma^4}{1-\gamma^4} - 0.0158\gamma^3.$$

In Eq. (A.1), $d$ and $D$ are in inches, $h_w$ is the differential air pressure in inches of water reading across the taps on the two sides of the orifice plate, and $\rho_f = 0.075\,\mathrm{lbm/ft^3}$ for air at standard temperature and pressure. The Reynolds number for the annulus is obtained by

$$\mathrm{Re} = \frac{Qh}{A_n \nu} = \frac{1}{2}\mathrm{Re}_{D_h}, \tag{A.2}$$

where the annular gap width is $h = 9.3\,\mathrm{mm}$, the kinematic viscosity of air $\nu = 1.62 \times 10^{-5}\,\mathrm{m^2/s}$, and $A_n = \pi(R_o^2 - R_i^2) = 2.87 \times 10^{-3}\,\mathrm{m^2}$ is the annular cross-sectional area.

## References

Arai, M., Tajima, K., 1998. Leakage-flow-induced vibrations of an axisymmetric body. Part 1: Analysis of the moment acting on an axisymmetric body for rotational motion. JSME International Journal 41, 347–354.

Arai, M., Tajima, K., 1999. Leakage-flow-induced vibrations of an axisymmetric body. In: Proceedings of the Asia-Pacific Vibration Conference, Vol. 2, pp. 991–996.

Bélanger, F., de Langre, E., Axisa, F., Païdoussis, M.P., Mateescu, D., 1994. Dynamics of coaxial cylinders in laminar annular flow by simultaneous integration of the Navier–Stokes and structural equations. Journal of Fluids and Structures 8, 747–770.

Chen, S.S., Wambsganes, M.W., Jendrzejczyk, J.A., 1976. Added mass and damping of a vibrating rod in confined viscous fluid. Journal of Applied Mechanics 43, 325–329.

Chorin, A.J., 1967. A numerical method for solving incompressible viscous flow problems. Journal of Computational Physics 2, 12–26.

Cooley, J.W., Lewis, P.A.W., Welch, P.D., 1969. The finite Fourier transform. IEEE Transactions on Audio and Electronics AU-17, 77–85.

De Langre, E., Porcher, G., Axisa, F., 1994. An experiment on fluidelastic instability in a confined annular flow. In: Proceedings 2nd International Conference on Engineering Aero-Hydroelasticity, Pilsen, Czech Republic, pp. 26–31.

Fujita, K., Ito, T., Kawata, Y., Izumi, H., 1994. Axial leakage flow-induced vibration of long flexible rod with small gaps. In: Au-Yang, M.K., Fujita, K. (Eds.), Flow-Induced Vibration, PVP-Vol. 273. ASME, New York, pp. 133–143.

Harlow, F.H., Welch, J.E., 1965. Numerical computation of time-dependent viscous incompressible flow of fluid with free surface. Physics of Fluids 8, 2182–2189.

Hobson, D.E., 1982. Fluid-elastic instabilities caused by flow in an annulus. In: Proceedings of 3rd International Conference on Vibration of Nuclear Plant, Keswick, UK. BNES, London, pp. 460–463.

Inada, F., Hayama, S., 1990. A study on leakage-flow-induced vibrations. Part 1: fluid dynamic forces and moments acting on the walls of a narrow tapered passage. Part 2: stability analysis and experiments for two-degree of freedom systems combining translational and rotational motions. Journal of Fluids and Structures 4, 395–412 and 413–428.

Li, D.W., Kaneko, S., Hayama, S., 2002. A study on annular leakage-flow-induced vibrations. Journal of Fluids and Structures 16, 909–930.

Mateescu, D., Païdoussis, M.P., 1985. The unsteady potential flow in an axially-variable annulus and its effect on the dynamics of the oscillating rigid center-body. ASME Journal of Fluids Engineering 107, 412–427.

Mateescu, D., Païdoussis, M.P., Bélanger, F., 1988. Unsteady pressure measurements on an oscillating cylinder in narrow annular flow. Journal of Fluids and Structures 2, 615–628.

Mateescu, D., Païdoussis, M.P., Bélanger, F., 1989. A theoretical model compared with experiments for the unsteady pressure on a cylinder oscillating in turbulent annular flow. Journal of Sound and Vibration 135, 487–498.

Mateescu, D., Païdoussis, M.P., Bélanger, F., 1994a. A time-integration method using artificial compressibility for unsteady viscous flows. Journal of Sound and Vibration 177, 197–205.

Mateescu, D., Païdoussis, M.P., Bélanger, F., 1994b. Unsteady annular viscous flows between oscillating cylinders. Part I: computational solutions based on a time integration method. Part II: a hybrid time-integration solution based on azimuthal Fourier expansions for configurations with annular backsteps. Journal of Fluids and Structures 8, 489–507 and 509–527.

Mateescu, D., Mekanik, A., Païdoussis, M.P., 1996. Analysis of 2-D and 3-D unsteady annular flows with oscillating boundaries based on a time-dependent coordinate transformation. Journal of Fluids and Structures 10, 57–77.

Mekanik, A., 1994. General solution for unsteady annular flows between concentric cylinders and annular flow-induced instabilities. Ph.D. Thesis, Department of Mechanical Engineering, McGill University, Canada.

Mekanik, A., Mateescu, D., Païdoussis, M.P., 1993. Computational solution of Navier–Stokes equations for annular flows with moving boundaries. In: Proceedings of 14th Canadian Congress of Applied Mechanics, Queen's University, Kingston, Ont., Canada, pp. 243–244.

Mekanik, A., Païdoussis, M.P., Mateescu, D., 1994. Pressure measurements in unsteady flows between concentric cylinders in translation and rotation. In: Proceedings of the 12th Symposium on Engineering Application of Mechanics, McGill University, Montreal, Qué., Canada, pp. 345–353.

Miller, D.R., 1970. Generation of positive and negative damping with a flow restrictor in axial flow. In: Proceedings of the Conference on Flow-Induced Vibrations in Reactor System Components. Argonne National Laboratory Report ANL7685, Argonne IL, USA, pp. 304–311.

Miller, R.W., 1989. Flow Measurement Engineering Handbook, second ed. McGraw-Hill, New York.

Païdoussis, M.P., 1980. Flow-induced vibration in nuclear reactors and heat exchangers: practical experiences and state of knowledge. In: Naudascher, E., Rockwell, D. (Eds.), Practical Experiences with Flow-induced Vibration. Springer, Berlin, pp. 1–81.

Païdoussis, M.P., 1998. Fluid–Structure Interactions, Slender Structures and Axial Flow, vol. 1. Academic Press, London.

Païdoussis, M.P., 2003. Fluid–Structure Interactions, Slender Structures and Axial Flow, vol. 2. Elsevier Academic Press, London.

Perotin, L., Granger, S., 1997. A linearized unsteady model for computing dynamics of cylindrical structures subjected to nonuniform annular flows at high Reynolds numbers. Journal of Fluids and Structures 11, 183–205.

Porcher, G., de Langre, E., 1997. A friction-based model for fluidelastic forces induced by axial flow. In: M.P. Païdoussis, et al. (Eds.), Proceedings 4th Int'l Symposium on Fluid–Structure Interactions, Aeroelasticity, Flow-Induced Vibration and Noise, Vol. II, AD-Vol. 53-2. ASME, New York, pp. 67–74.

Soh, W.Y., 1987. Time-marching solution of incompressible Navier–Stokes equations for internal flows. Journal of Computational Physics 70, 232–252.

Soh, W.Y., Goodrich, J.W., 1988. Unsteady solution of incompressible Navier–Stokes equations. Journal of Computational Physics 79, 113–134.

Spurr, A., Hobson, D.E., 1984. Forces on the vibrating centrebody of an annular diffuser. In: Païdoussis, M.P., Au-Yang, M.K. (Eds.), ASME Symposium on Flow-Induced Vibration; Vol. 4: Vibration Induced by Axial and Annular Flows. ASME, New York, pp. 41–52.

Tanaka, S., Hirata, T., Kaneko, S., Watanabe, T., 2001. Aerodynamic vibration of combined rigid bodies due to leakage-flow. In: Pettigrew, M.J. (Ed.), Flow-Induced Vibration-2001. Vol. 2, PVP-Vol. 420-2. ASME, New York, pp. 45–52.

Thompson, J.F., Warsi, Z.U.A., Wayne Mastin, C., 1985. Numerical Grid Generation: Foundations and Applications. Elsevier Science, New York.

Vinokur, M., 1983. On one-dimensional stretching functions for finite-difference calculations. Journal of Computational Physics 50, 215–234.